Chemical Engineering Science 66 (2011) 426–439

Contents lists available at ScienceDirect

Chemical Engineering Science

journal homepage: www.elsevier.com/locate/ces

Drop rise velocities and fluid dynamic behavior in standard test systems for liquid/liquid extraction—experimental and numerical investigations

K. Bäumler [a,*], M. Wegener [b], A.R. Paschedag [c], E. Bänsch [a]

[a] Chair of Applied Mathematics III, Friedrich-Alexander-Universität, Haberstraße 2, D-910548 Erlangen-Nürnberg, Germany
[b] Chair of Chemical and Process Engineering, Technische Universität Berlin, Ackerstraße 71-76, D-13355 Berlin, Germany
[c] University of Applied Sciences Berlin, Luxemburger Str. 10, D-13353 Berlin, Germany

ARTICLE INFO

Article history:
Received 30 July 2010
Received in revised form
27 September 2010
Accepted 2 November 2010
Available online 11 November 2010

Keywords:
Drop
Terminal velocity
Dynamic simulation
Multiphase flow
Aspect ratio
Interface

ABSTRACT

The fluid dynamic behavior of single organic droplets rising in a quiescent ambient liquid is investigated experimentally and numerically. Three standard test systems for liquid/liquid extraction recommended by the European Federation of Chemical Engineering (EFCE) but without the respective transfer component have been chosen for the investigations: toluene/water, *n*-butyl acetate/water, and *n*-butanol/water, representing systems with high, medium, and low interfacial tension. Simulations are performed using the academic code Navier, which features a sharp interface representation and a variational formulation of the curvature. The validity of both correlations and the results obtained by dynamic numerical simulation is discussed in terms of terminal rise velocity, aspect ratio, and the onset of shape oscillation. The numerical results show excellent agreement with experiments in all three test systems, and with simulations in the *n*-butanol/water system published recently by Bertakis et al. (2010). The presented numerical method is applicable for a wide range of interfacial tension, whereas the investigated correlations lose accuracy with decreasing interfacial tension.

1. Introduction

The velocity of droplets is a crucial and important parameter in many industrial applications, particularly in liquid/liquid extraction processes where one liquid phase is dispersed in an ambient liquid. Freely rising or falling single droplets rarely occur in industrial equipment due to several reasons such as swarm or wall effects, influence of mass transfer or influence of internals, etc. Nevertheless, the free rise or fall of single droplets in a fluid of unrestricted extent is the basis of all further modelling approaches and thus an important design parameter.

Typically, the terminal velocity is determined as a function of the droplet diameter. Very small fluid particles, i.e. droplets with a sufficiently small Weber number $We = u_t^2 d_P \rho_c / \sigma$, are spherical in shape. In this regime, the drag depends mainly on viscosity and density ratio, μ^* and ρ^*, respectively, and a possible contamination due to surfactants (Loth, 2008). Especially small droplets are sensitive to contaminants, thus in unpure conditions the surface can be regarded as rigid (e.g. Clift et al., 1978). In carefully purified systems, however, even small fluid particles have an inner circulation due to the momentum transfer exerted by the outer fluid on the droplet interface. The drag is reduced compared to a rigid particle and drop velocity rises significantly.

When the droplet diameter increases, the velocity increases as well until the peak or maximum velocity is attained. In many cases, droplet shape is oblate ellipsoidal at this stage. The drag increases sharply and drop velocity decreases with increasing diameter. At a critical Weber number around $We=4$ (Hu and Kintner, 1955; Krishna et al., 1959; Winnikow and Chao, 1966), the droplet starts to oscillate periodically until the wobbling regime begins, where droplets exhibit irregular shape deformations (Clift et al., 1978).

An analytical solution for the Navier–Stokes equations derived by Hadamard (1911) and Rybczynski (1911) exists only in the creeping flow regime. For higher Reynolds numbers, one has to apply correlations or numerical methods to predict the terminal velocity of droplets in a given system. In terms of correlations, there are several options:

- Use of generalized graphical correlations plotting the Reynolds number at steady state versus the Eötvös number for different Morton numbers as proposed e.g. by Grace et al. (1976). The correlation is given in double logarithmic scale and can be used for a first estimation. It should not be applied to systems with extreme density or viscosity ratios.
- Calculation of the terminal velocity using correlations expressed in dimensionless form based on a variety of experimental data as proposed e.g. by Hu and Kintner (1955) or Grace et al. (1976).

* Corresponding author. Tel.: +49 9131 8525230; fax: +49 9131 8525228.
E-mail addresses: baeumler@am.uni-erlangen.de (K. Bäumler), mirco.wegener@tu-berlin.de (M. Wegener), anja.paschedag@tfh-berlin.de (A.R. Paschedag), baensch@am.uni-erlangen.de (E. Bänsch).

0009-2509/$ - see front matter © 2010 Elsevier Ltd. All rights reserved.
doi:10.1016/j.ces.2010.11.009

These correlations are valid for contaminated systems only and a semi-empirical correction for pure systems is needed as proposed e.g. by Grace et al. (1976). This semi-empirical approach was recently applied by Wegener et al. (2010) for the toluene/water system. Some correlations permit to calculate the velocity of oscillating droplets in clean systems (e.g. Thorsen et al., 1968). The model proposed by Henschke (2004) (see Appendix A) is valid for spherical, deformed and oscillating droplets, but five parameters have to be determined to characterize a given system.

- Indirect determination of terminal velocities by plotting drag coefficient versus Reynolds number, using the viscosity ratio as a parameter. A variety of correlations exists, amongst others e.g. Hamielec et al. (1963), Feng and Michaelides (2001), Rivkind and Ryskin (1976), and Saboni and Alexandrova (2002). The main shortcomings are the restricted validity range in terms of the Reynolds number, and the applicability to spherical droplets only. Furthermore the correlations differ significantly among each other.

All methods are only valid at equilibrium conditions, i.e. at terminal velocity. For non-equilibrium conditions, correlations for dynamic parameters have to be identified, see Loth (2008) for further details. The main difficulty of the above-mentioned methods is to judge which one should be used for a given system. The validation with and the comparison to experimental data are oftentimes difficult since the degree of contamination is unknown or not specified by the authors. The advantage of CFD methods is apparent: the interface in the simulations is inherently "clean" or free of contaminants. If experiments under clean conditions and numerical simulations coincide, an important step is made to predict terminal velocities in liquid/liquid systems.

However, numerical simulations of single drop rise or fall in liquid medium are rare in literature. Deshpande and Zimmerman (2006) present a level set approach to study the shape of droplets in a wide range of Morton and Eötvös numbers, $Mo = 10^{-4} \ldots 10^{4}$ and $Eo = 3.6 \ldots 360$, respectively, at Reynolds numbers around 10. The results obtained in the simulations show that the generalized graphical correlation by Grace et al. (1976) can be adopted for describing droplet shape in a reasonable manner.

Petera and Weatherley (2001) investigate the fall velocity of water droplets enriched with ethanol in *n*-decanol (and mass transfer across the interface as well, but this is not the focus here), a low interfacial tension system with Reynolds numbers between 10 and 30 and droplet sizes roughly between 3.1 and 4.6 mm. They compare own experimental data with FEM simulations using the Lagrangian framework with automatic remeshing in 2D-axisymmetric flow. Results show that terminal velocities and droplet shapes are well predicted by the numerical model. The terminal velocity is attained relatively quickly in less than a second which was confirmed by the experiments.

Watanabe and Ebihara (2003) compare the rising velocities of single droplets with two types of empirical correlations using the lattice Boltzmann method. Reynolds, Eötvös, and Morton number of the investigated system are 15.8, 5.07, and 1.27×10^{-3}, respectively. Following the general graphical correlation by Grace et al. (1976), the droplet shape should be ellipsoidal, which is confirmed by the simulations. The terminal velocity agrees well with a correlation given by Grace et al. (1976) (see Appendix A) which is valid explicitly for contaminated systems only. The authors do not comment on this issue and give no hints on internal circulations in the droplet.

Waheed et al. (2004) solve the governing equations with the finite element method to calculate the sedimentation velocity of spherical liquid droplets in axisymmetric steady flow. Results for the limiting cases $\mu^* \to 0$ and $\mu^* \to \infty$ show reasonable agreement compared to the drag coefficient models by Feng and Michaelides (2001) and Rivkind et al. (1976). Comparisons to experimental data from Thorsen et al. (1968) show partly good agreement for small diameters in the ethylene bromide/water system but less agreement in the carbon tetrachloride/water system. Deformable droplets cannot be represented by their numerical method.

A 3D front tracking model has been applied by Dijkhuizen et al. (2005) to simulate the rise of toluene droplets in water. The droplet size was varied between 4 and 12.5 mm. Plots of the drop rise velocity versus time show that the velocity is nearly the same for all diameters. A sinusoidal oscillation appears for droplets bigger than 5 mm, the amplitude being higher for larger droplets. But comparisons with experimental data recently published by Wegener (2009) and Wegener et al. (2010) show that the frequency of the oscillations seems to be rather unrealistic. The terminal drop rise velocities calculated by Dijkhuizen et al. (2005) will be compared with own simulations in the Results and Discussion Section.

Wegener et al. (2009) use the commercial CFD-code STAR-CD to simulate unsteady mass transfer and the transient drop rise velocity with simultaneous interfacial instabilities for spherical droplets in a fully 3D model. Simulations without mass transfer in the system toluene/water have also been performed. The terminal drop rise velocity is in good agreement up to 3 mm droplets, larger droplets deform and the numerical method is not able to capture the relevant physical effects.

Bertakis et al. (2010) investigate the *n*-butanol/water system – a low interfacial tension system – experimentally and numerically. In the numerical investigations, the 3D finite element package DROPS (Groß et al., 2006) is used, the interface is captured with the level set method. The computational domain is 3D. The droplet sizes cover the range from spherical, deformed to oscillating regime. Simulation results for five different diameters are presented which are in excellent agreement with the curve for an ideally mobile interface. The time scale of the simulations is rather short and does not exceed 0.7 s, thus the oscillation frequency is not fully developed. Hence it is not clear in which manner the code is able to handle oscillatory effects, especially for larger, strongly deformed droplets.

The objective of this study is to present a finite element method that can be used for simulating systems with low, medium and high interfacial tension. The standard test systems *n*-butanol/water (low interfacial tension), *n*-butyl acetate/water (medium interfacial tension), and toluene/water (high interfacial tension) have been chosen for this purpose. Numerical simulations of a single droplet – initially at rest and accelerating according to the acting forces – rising in an ambient liquid are performed with the academic FEM-code Navier which uses a sharp interface representation in a mesh moving method. In such a method, nodes associated to the interface are moving according to the deformation of the interface. This leads to a grid movement and has to be accounted for in the governing equations. A drawback of the currently used mesh moving method is its inability to capture changing topologies like droplet coalescence or breakup. Level set methods and volume of fluid methods work on a fixed grid, and determine the position of the interface with the aid of an additional scalar balance equation. Both methods, level set and volume of fluid, are able to capture topology changes, which makes them an adequate choice for many applications. In the present application, in the considered diameter ranges of the droplets, topology changes do not arise. Furthermore level set and volume of fluid methods require a reconstruction of the interface, whereas in the mesh moving method the interface is given explicitly. On an explicitly given interface the surface forces can be calculated with a higher accuracy, which leads to an exact capture of surface forces in a wide range of interfacial tensions, and thus to an exact capture of rise velocities and aspect ratios. The interfacial conditions are implemented using the Subspace Projection Method (SPM). Further characteristics are a co-moving frame of reference and a variational formulation of the curvature providing an effective method for a

consistent, very exact description of discrete surface stresses. Numerical results are compared to the experimental and numerical data for *n*-butanol droplets in water by Bertakis et al. (2010), to experimental data for toluene droplets in water recently published by Wegener et al. (2010) and to own experiments in the *n*-butyl acetate/water system performed for this study.

The strategy is as follows: in the next section the experimental data of terminal drop rise velocities plotted versus the droplet diameter are presented and compared to correlations from literature. The model proposed by Henschke (see Bertakis et al., 2010; Henschke, 2004) is then applied to derive an equation that is continuous over the considered diameter range. Thereto, the free model parameters are fitted to the experimental data. Then the numerical method is described in detail. Shapes and aspect ratios are investigated for all three systems. Finally, the simulated drop rise velocity is compared to the Henschke model, representing the experimental data.

2. Experimental investigations

The experimental setup is the same as described in Wegener et al. (2010) for the toluene/water measurements and is only shortly repeated here (see Fig. 1) to describe the *n*-butyl acetate measurements made for this study. The instantaneous drop rise velocity is measured in a glass column (h=1000 and 75 mm in diameter). The column (1) is equipped with a planar jacket (2) in order to allow for optical access. The temperature of the system is adjusted to 25 °C by a LAUDA thermostat (3). A precision dosing pump (Hamilton PSD/2 module) (4) generates droplets of desired diameter at a nozzle (5). Droplet release is realized with a solenoid device (6). Two nozzles have been used: one glass nozzle (inner diameter 0.5 mm) for small and intermediate droplet sizes, and a stainless steel nozzle (inner diameter 2 mm) for larger droplets.

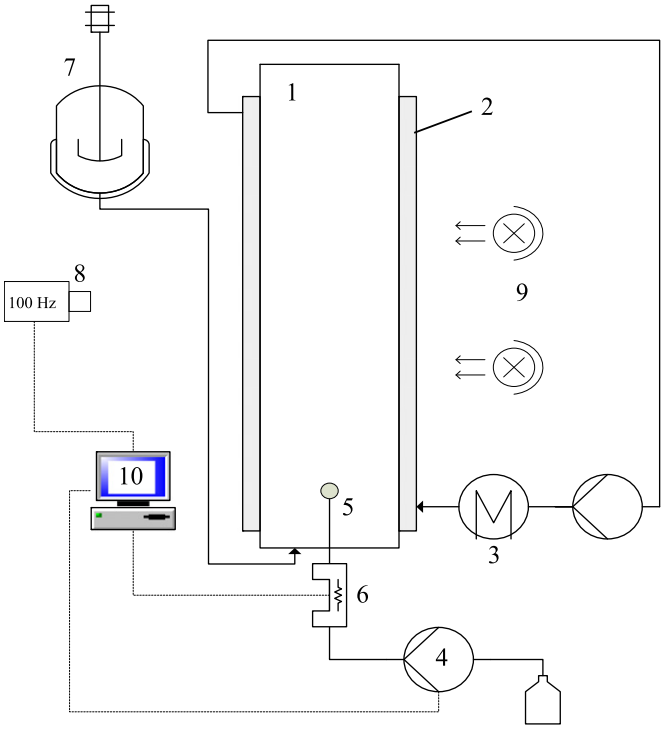

Fig. 1. Experimental setup. (1) Glass column, (2) jacket, (3) thermostat, (4) precision dosing pump, (5) nozzle, (6) solenoid device, (7) saturation tank, (8) high speed camera, (9) illumination system, (10) computer control.

The organic and aqueous phase are mutually saturated in a stirred tank (7) to avoid mass transfer between both phases. Since the system is very sensitive to impurities, a precise cleaning procedure has been accomplished. In addition, only chemicals of high purity have been used: *n*-butyl acetate p.a. $\geq$ 99.5% provided by Merck, the continuous phase is highly purified deionized water with a specific resistance of 18.3 MΩ cm. The physical properties are calculated from data published by Misek et al. (1985) and summarized in Table 1.

Droplet movement is recorded with a high speed camera (Photonfocus MV-752-160) with a frame rate of 100 Hz. The camera position is perpendicular to the column, and the entire particle path through the column can be captured. In a next step, an image processing tool (Image-Pro Plus 5.1 by Media Cybernetics) for image analysis is used. As a result, the vertical and horizontal position of the mass center of the drop for each frame is obtained, and the instantaneous drop rise velocity can be calculated.

As shown in Table 1, droplet diameters were varied from 1.0 to 4.5 mm in the *n*-butyl acetate/water system. All experiments for a certain droplet diameter were repeated at least 15 times to satisfy statistical significance. Two different terminal velocity values are then calculated for each diameter according to Wegener et al. (2010), see also Fig. 2: a maximum velocity u_{max} and a characteristic mean velocity u_{cha}. The maximum drop rise velocity is the mean of all maximum velocities of the 15 recorded sequences for one droplet diameter. The characteristic mean velocity is calculated by dividing the travel distance h_{tr} by the time Δt needed to pass h_{tr}. The travel distance begins after the acceleration stage is over and ends when the upper end of the column was reached. All characteristic mean velocities of all recorded sequences of one diameter are then averaged. In general, excellent reproducibility was found in all measurements. The velocity values are given in Tables B4–B6 in Appendix B for each test system.

2.1. Experimental results and correlations

Fig. 3 shows the terminal drop rise velocities in the toluene/water system (data by Wegener et al., 2010). The lower limit of the horizontal bars represents the characteristic mean velocity u_{cha}, the upper limit the maximum velocity u_{max}, i.e. if the distance between the bars is small, the u_{cha} and u_{max} values are close to one another

Table 1
Physical parameters of the binary systems toluene/water and *n*-butyl acetate/water at ϑ = 25 °C, *n*-butanol/water at 20 °C.

	ρ (kg/m^3)	μ (mPa s)	σ (mN/m)	*Mo* (–)	d_P range (mm)	Data source
Toluene$_{(d)}$	862.3	0.552	35	1.95×10^{-11}	1…7	Wegener et al. (2010)
Water$_{(c)}$	997.02	0.8903				
n-Butyl acetate$_{(d)}$	877.19	0.82	14	2.87×10^{-10}	1…4.5	This study
Water$_{(c)}$	996.6	0.904				
n-Butanol$_{(d)}$	845.44	3.28	1.63	1.23×10^{-6}	1…4	Bertakis et al. (2010)
Water$_{(c)}$	986.51	1.39				

which means that there are no significant oscillations in the velocity. In contrast, if there is a larger distance, as can be seen in the diameter range 2.4…3.0 and >4.5 mm, velocity oscillations appear. For the droplets with $d_P > 4.5$ mm, this is due to shape deformations. The critical diameter d_{cr}, at which shape oscillations set in, can be predicted by a correlation given by Klee and Treybal (1956) (originally, d_{cr} was meant to divide the spherical regime, where the velocity increases with diameter, from the regime of deformable droplets, where velocity remains substantially constant or slightly decreases with droplet diameter):

$$d_{cr} = 1.77\rho_c^{-0.14}\Delta\rho^{-0.43}\mu_c^{0.3}\sigma^{0.24} \quad (1)$$

For toluene/water Eq. (1) yields d_{cr}=4.45 mm, exactly at the experimentally determined onset of oscillations. Fig. 4 shows photographs of toluene droplets rising in water for different droplet diameters (d_P=4.0, 4.5, 5.0 and 6.0 mm). Four mm droplets are deformed, but droplet shape remains practically constant and no shape oscillations occur. For 4.5 mm droplets, a regular shape oscillation can be stated. The drop rising path, however, is vertical, only small deviations from the column axis were observed. The shape of 5 and 6 mm droplets becomes more and more deformed, the oscillatory behavior is quite irregular and significant deviations from the vertical axis occur.

In the diameter range 2.4…3.0 mm, velocity oscillations appear which are not due to shape deformation or contamination effects. The droplets are nearly spherical and the corresponding Weber number is lower than the critical value We=4 (which indicates the onset of deformation). In addition, at d_P=3.0 mm, a bifurcation effect appears comparable to the findings of Thorsen et al. (1968). The reason remains unclear, for further details we refer to the discussion in Wegener et al. (2010).

The comparison in Fig. 3 with the correlation for contaminated systems given by Grace et al. (1976) (see Appendix A) shows that the experimental data reflects a pure system. Even the smallest diameter exhibits higher velocities than predicted by the model which indicates internal circulations. The terminal velocities calculated from the drag coefficient correlation by Hamielec et al. (1963)

$$C_D = \frac{3.05(783\mu^{*2}+2142\mu^{*}+1080)}{(60+29\mu^{*})(4+3\mu^{*})Re^{0.74}} \quad (2)$$

show excellent agreement for droplets up to 3 mm with a deviation in the range of 5% even though Eq. (2) is only valid for $4 < Re < 100$.

In the oscillatory regime, the terminal drop rise velocity is proportional to $d_P^{-0.5}$. Thorsen et al. (1968) propose the following

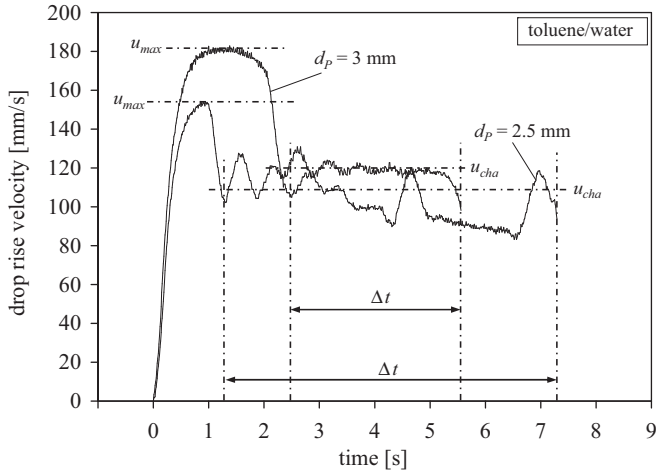

Fig. 2. Scheme for determination of maximum and characteristic mean velocity, u_{max} and u_{cha}.

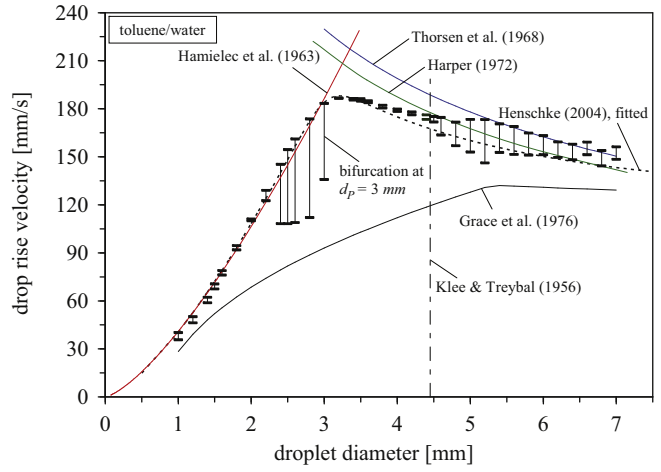

Fig. 3. Drop rise velocities of toluene droplets in water as a function of droplet diameter at $\vartheta = 25$ °C (Wegener et al., 2010). For comparison, correlations from literature are given in the figure, see text for further details.

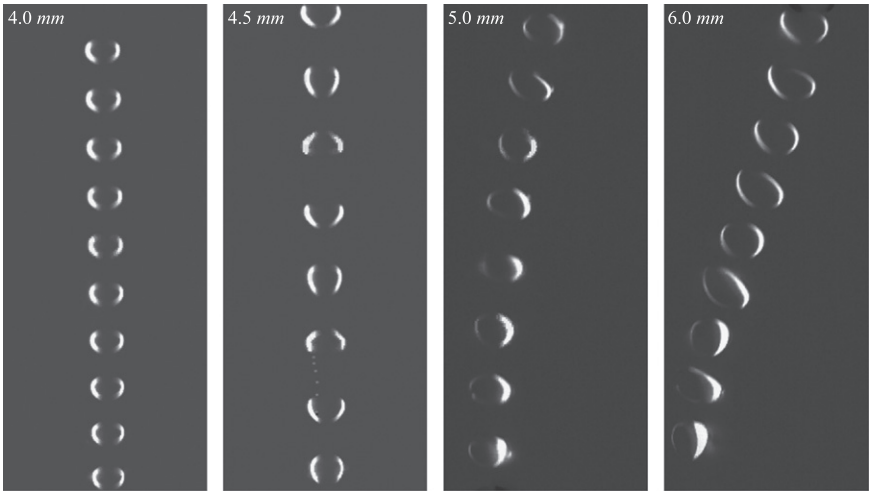

Fig. 4. Droplet shape of toluene droplets with different diameters rising in water.

equation which is also plotted in Fig. 3:

$$u_t = \frac{6.8}{1.65 - \frac{\Delta\rho}{\rho_d}} \frac{\sqrt{\frac{\sigma}{3\rho_d + 2\rho_c}}}{\sqrt{d_P}} \tag{3}$$

The agreement with the upper bound of velocities is good for droplets ≥ 5 mm. Following Harper (1972), the drag coefficient for particles with $We = 4$ can be expressed by

$$C_D = \frac{Mo\, Re^4}{48} \tag{4}$$

The respective terminal velocities calculated from Eq. (4) are plotted in Fig. 3 and show fairly good agreement in the oscillatory regime ($d_P > d_{cr}$). The different correlations envelop the experimental data, only the transition region between spherical and oscillating droplets cannot be described by the models.

In Fig. 5, the drop rise velocities of *n*-butyl acetate droplets in water are shown and compared to the correlations mentioned above. In contrast to the toluene/water system, no bifurcation effects were detected. The system is again relatively clean if the data are compared with the curve given by Grace et al. (1976). The critical diameter d_{cr} calculated with Eq. (1) is 3.78 mm and corresponds well with experimental findings. One can see that the amplitude of velocities in the oscillatory regime is smaller compared to toluene/water. Eqs. (2)–(4) envelop again the experimental data in a satisfactory manner.

Fig. 6 shows that the correlations (3) and (4) are not able to describe the *n*-butanol system despite low Reynolds numbers and Eötvös numbers within the validity range. Furthermore, the terminal velocities of the *n*-butanol system lie well below the correlation for contaminated systems given by Grace et al. (1976). The disagreement cannot be explained by contaminations since the authors paid much attention to keep the system clean. Probably, the higher viscosity ratio with high absolute viscosities in combination with a very low interfacial tension is critical in applying the correlations. The correlation given by Hamielec et al. (1963), Eq. (2), shows good agreement for small drop diameters. Due to low interfacial tension, deformation sets in at a relatively small diameter (compared to the other two investigated systems) and thus decreasing the validity range of Eq. (2). As a consequence, only CFD methods seem to be applicable in this case.

Henschke (2004) proposes a model which gives a continuous function over the whole diameter range (see Appendix A).

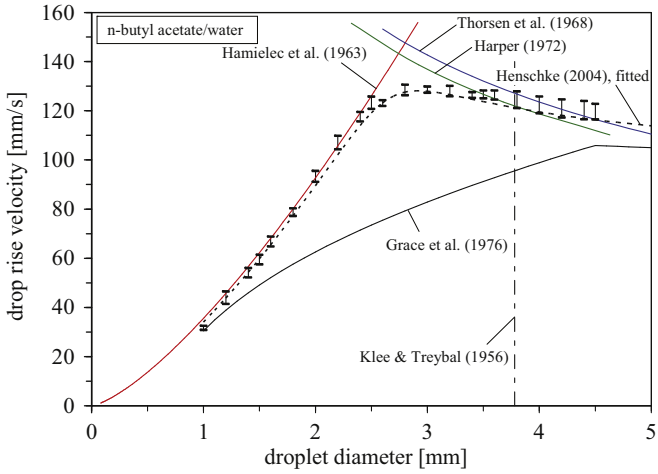

Fig. 5. Drop rise velocities of *n*-butyl acetate droplets in water as a function of droplet diameter at $\vartheta = 25\ ^\circ$C. For comparison, correlations from literature are given in the figure, see text for further details.

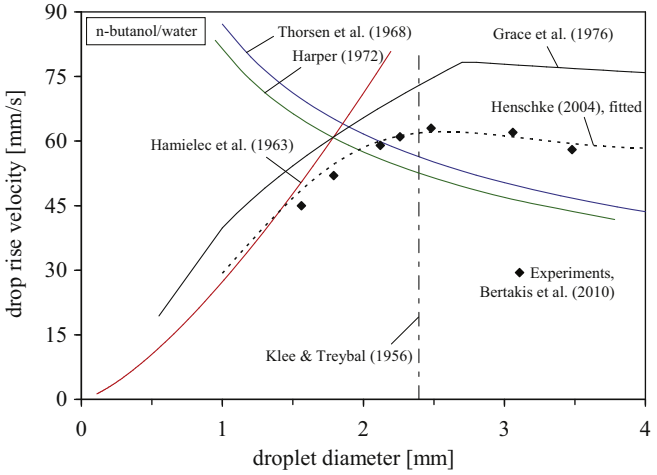

Fig. 6. Drop rise velocities of *n*-butanol droplets in water as a function of droplet diameter at $\vartheta = 20\ ^\circ$C (Bertakis et al., 2010). For comparison, correlations from literature are given in the figure, see text for further details.

Table 2
List of parameters used for the Henschke model.

	p_1 (mm)	p_2 (–)	p_3 (–)	p_4 (–)	p_5 (–)
Toluene/water	8.87	1.60	12.32	9.25	2.03
n-Butyl acetate/water	37.57	1.40	9.36	23.78	1.54
n-Butanol/water	1.63	3.76	2.98	10.00	8.00

The original model has five parameters $p_1,\ldots,p_5$, but two of them were constant in the respective investigations by Bertakis et al. (2010). In the present study, all five parameters are regarded as free parameters in order to get the best approximation to the experimental data. The parameters are obtained by the least square method and are given in Table 2. For the fitting procedure, the values in the second row in Tables B4 and B5 (characteristic mean values u_{cha}, except for $d_P = 2.4 \ldots 3$ mm in Table B4: u_{max} values) and B6 ($u_{t_{exp,Bertakis}}$) have been used. The resulting curve is drawn in Figs. 3, 5 and 6 as a dotted curve. They are used in the next chapter to compare experimental results with those from simulations.

3. Mathematical model and numerical method

The simulations have been performed with the academic code Navier (Bänsch, 2001; Bänsch et al., 2004a–c; Bänsch and Schmidt, 2000). In this section a short overview of the governing equations will be given, followed by the description of the most interesting aspects of the implementation of the two-phase flow problem within Navier.

3.1. Equations for two-phase flow

We consider two immiscible, Newtonian, incompressible fluids at a given, constant temperature. A sharp interface Γ between the immiscible fluids is assumed, and in the interior of each subdomain Ω_c or Ω_d assigned to the continuous or dispersed phase, respectively, the Navier–Stokes equations hold:

$$\rho_j \partial_t \mathbf{u}_j + \rho_j (\mathbf{u}_j \cdot \nabla)\mathbf{u}_j - \mu_j \Delta \mathbf{u}_j + \nabla p_j = \rho_j \mathbf{g} \quad \text{in } \Omega_j, \tag{5a}$$

$$\nabla \cdot \mathbf{u}_j = 0 \quad \text{in } \Omega_j \tag{5b}$$

for $j \in \{c,d\}$. At the interface Γ, the equations for the bulk-phases are coupled via jump conditions for the momentum flux and the velocity. Using the notation $[\cdot]$ for the jump of a quantity across the

interface, the equations read:

$$[\mathbf{u}] = 0 \quad \text{on } \Gamma, \tag{6a}$$

$$[T]\boldsymbol{\nu} = \sigma\kappa\boldsymbol{\nu} \quad \text{on } \Gamma, \tag{6b}$$

where T denotes the stress tensor for Newtonian fluids $T := \mu(\nabla\mathbf{u} + \nabla\mathbf{u}^\top) - pI$, κ is the sum of principal curvatures, and $\boldsymbol{\nu}$ the outer unit normal to Γ. The so-called *no-slip* condition (6a) states the continuity of the velocities at the interface. Note here that the gradients of the velocity are not continuous in general. Eq. (6b) specifies the momentum flux across the interface i.e. the jump of stresses. More precisely, (6b) reveals that forces in normal direction exerted by the fluid on the interface are balanced via the interfacial tension force $\sigma\kappa\boldsymbol{\nu}$. In tangential direction, the forces exerted on the interface Γ by the continuous phase equal the forces exerted by the dispersed phase.

An important part of the mathematical model is the time dependency of the domains. Ω_j should be understood as a time dependent domain $\Omega_j(t)$ throughout this paper. The same holds for the interface $\Gamma = \Gamma(t)$. The reason for this time dependency is the movement and deformation of the dispersed phase through the ambient liquid. In the mathematical model the time dependency of the domains is incorporated via the kinematic condition (7) that describes the movement of the interface via the interface velocity V_Γ in normal direction:

$$V_\Gamma = (\mathbf{u}|_\Gamma \cdot \boldsymbol{\nu})\boldsymbol{\nu} \quad \text{on } \Gamma. \tag{7}$$

3.2. Numerical method

The crucial part in simulating deformable droplets rising (or falling) in a quiescent liquid is the exact capture of the interfacial condition (6b), which includes the discrete curvature. Further difficulties comprise the discontinuity of the pressure across the interface, i.e. a representation of discontinuous functions in the finite element setting is needed, and the relatively large distance a droplet covers until it reaches its terminal velocity.

In order to exactly capture the velocity and pressure, a mesh moving method is used. Thus, vertices of the triangulation lie on the interface and move along with it. In the finite element context, one possibility of representing discontinuous functions can be realized via (logically) doubled nodes on the interface, where one node is associated with the continuous phase, the doubled node is associated with the dispersed phase.

In the mesh moving context, the nodes lying on the interface follow the motion of the droplet. To avoid a severe distortion of the mesh, a moving reference frame is used. The idea is to fix the origin of the coordinate system to the barycenter of the droplet, and accelerate it in time until the droplet reaches its steady state, the terminal velocity. Due to the acceleration of the coordinate system the governing equations in this moving reference frame are altered. The concept of the moving reference frame has been discussed by Maxey and Riley (1983), applications can be found in Wang et al. (2008), Wegener et al. (2009), and Weking and Weigand (2008).

The time dependent transformation Φ of the coordinate system is obtained by a translation in z-direction (direction of gravitational force, a sketch of the coordinate system is found in Fig. 7). It equals the movement of the barycenter of the droplet $\mathbf{x}_B(t)$, which is given at any time as the mean value integral over the domain of the droplet:

$$\Phi(\mathbf{x},t) := \mathbf{x} - \mathbf{x}_B(t) \quad \text{with } \mathbf{x}_B(t) = \fint_{\Omega_d} \mathbf{x} \tag{8}$$

To determine the velocity of the barycenter, we consider Newton's second law:

$$\ddot{\mathbf{x}}_B(t) = g + \frac{1}{\varrho_d} \int_{\partial\Omega_d} T_c\boldsymbol{\nu} \tag{9a}$$

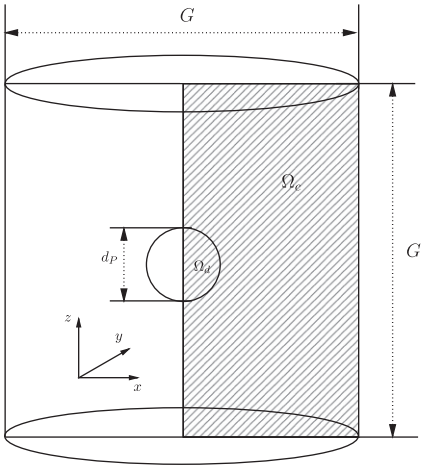

Fig. 7. The shaded area represents the computational domain for the axisymmetric setting. Ω_c is the domain covered by the continuous phase, Ω_d is the domain of the drop. G is the height of the computational domain. For the simulations $G = 12d_P$ was chosen.

For deformable droplets we can make use of the interfacial condition (6b). By applying Gauss's theorem to the right hand side of Eq. (9a) and inserting (6b), we obtain

$$\ddot{\mathbf{x}}_B(t) = \frac{d}{dt} \fint_{\Omega_d} \mathbf{u}(\mathbf{x},t) \tag{9b}$$

With respect to the initial condition (stating that the drop starts from rest):

$$\fint_{\Omega_d} \mathbf{u}(\mathbf{x},0) = 0 \tag{10}$$

we solve the ordinary differential equation (9a) for spherical and rigid drops (see also Wegener et al., 2009), and (9b) for deformable drops. The latter approach was also used by Wang et al. (2008). The use of the moving reference frame implies that the droplet does not move through the computational domain, only the deformation of the droplet is captured by the mesh. This leads to a significantly smaller movement of mesh nodes. Nevertheless, a smoothing of the grid is needed after every altering of node-coordinates. To further increase the accuracy of interfacial quantities, an isoparametric piecewise quadratic representation of the free boundary edges is used.

A main feature of the interface representation in NAVIER is the variational curvature formulation. This method was first analyzed by Dziuk (1988), and then considered in the Navier–Stokes context by Bänsch (2001). This variational formulation avoids the explicit evaluation of the *discrete* curvature and captures interfacial tension very accurately.

The interfacial conditions (6) are realized via the Subspace Projection Method (SPM). The SPM is based on the idea of a Petrov–Galerkin method on suitable subspaces. By the adept choice of these subspaces the interfacial condition (6b) is inherited in the numerical method as natural boundary condition on Γ while condition (6a) is fulfilled by restricting solutions to a space of functions yielding this condition. The SPM has been utilized in a related setting by Prignitz and Bänsch (2010). As a byproduct, the SPM results in a linear system of equations that is solved for both phases simultaneously via an iterative GMRES solver.

Further characteristics of the numerical implementation are the fractional-step-θ scheme with operator splitting for time discretization, and Taylor–Hood elements for spatial discretization (i.e. piecewise quadratic elements for the velocity space, and piecewise linear elements for the pressure space). Since it is advantageous for the chosen application to use an explicit treatment of the free

boundary, a CFL condition, i.e. a time step restriction, has to be fulfilled. The simulations were performed in a rotationally symmetric setting, which allows to solve the equations on a 2D mesh. Consequently, the simulated droplet rises in the direction of the z-axis only (compare Fig. 7 for the orientation of the coordinate system). Deviations of the rising path in the x,y-plane, as observed in experiments for larger droplets (see Fig. 4), are not captured by the rotationally symmetric setting.

3.3. Setup of the simulations

Simulations of the three different test systems are performed with the above described code Navier. The parameters of the implementation are chosen according to Table 1. Special care was taken when the grid for the simulations was created. A sketch of the chosen geometry is given in Fig. 7. A slice of the 3D domain is used for the axisymmetric simulation. The computational domain Ω is rectangular with the width $G/2$ and the height G. To minimize grid-dependence, different geometries and refinements of grids have been tested. A computational domain with $G = 12d_P$ consisting of approximately 4000 triangles showed no more wall-effects that may lead to lower rise velocities of the droplets. The refinement is higher close to the interface and a representation of the free boundary by 59 edges (each containing a midpoint-node, due to the use of quadratic elements) was found sufficient to capture interfacial tension. The grid close to the interface is plotted in Fig. 8.

As mentioned above, the time step size has to fulfill a CFL condition. In the present applications a fixed time step size in the order of 10^{-5} s was found to be sufficiently small.

The simulations comprise the acceleration stage of the droplet, surrounded by initially quiescent liquid, until a steady state is reached. The simulated time span is at least twice the time necessary for reaching terminal velocity. In general, 60 000 time steps were computed.

To mention a known problem in mesh moving methods we want to point out that our simulations, due to the small time step size, show no significant volume loss or gain. A plot of the relative volume V_{drop}/V_0 evolving over time can be seen in Fig. 9 in the test system n-butanol/water. Three different initial diameters of droplets were checked for possible volume loss. The results reveal that the smaller the deformation of the droplets, i.e. the smaller the diameter of the droplets, the more accurately the volume is captured. But even for small aspect ratios, as they arise for example for a 3 mm n-butanol droplet rising in water (their steady state is at an aspect ratio of $E=0.36$, see Table B7), the volume is captured very accurately, since the deviation is less than 0.025%. The largest volume gain of all simulations was found for the 4.4 mm oscillating toluene drop, where a deviation of less than 0.15% was determined.

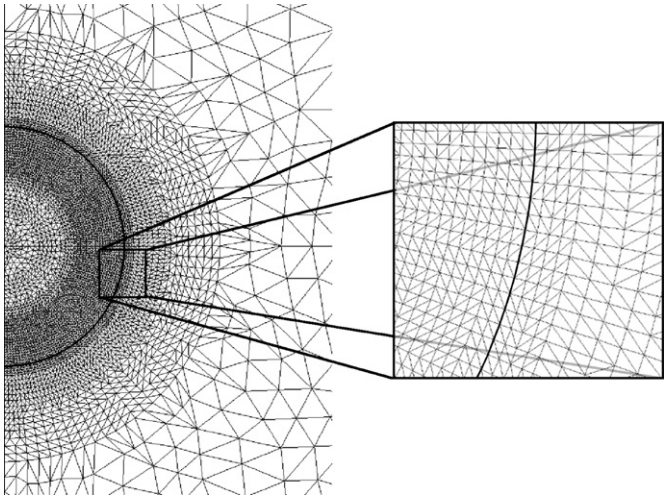

Fig. 8. Detail of the computational mesh close to the interface (left part) with additional zoom to the interfacial region (right part). The refinement is significantly higher close to the interface (indicated by a thick black line) and inside the droplet, where the highest gradients occur.

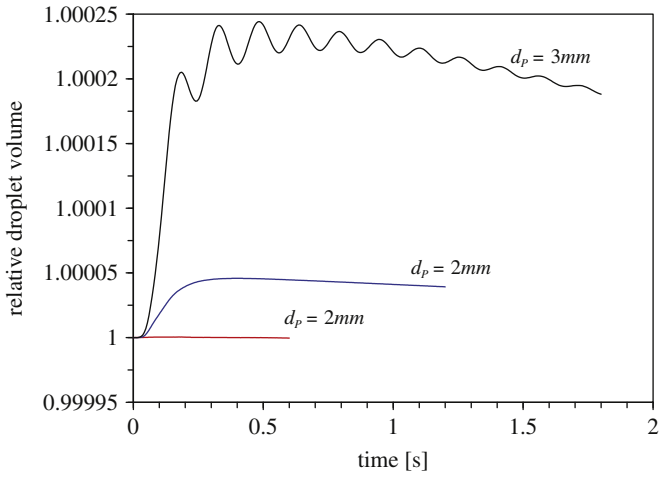

Fig. 9. Simulated relative volume V_{drop}/V_0 of n-butanol droplets rising in water.

4. Results and discussion

The numerical results are compared to own experimental data in the system toluene/water and n-butyl acetate/water. In the system n-butanol/water the simulations of Navier are compared to experimental and numerical data published recently by Bertakis et al. (2010).

Simulations with Navier comprise the acceleration stage of droplets from rest and initially spherical shape until a steady state is reached. In the case of oscillating droplets, simulations run until oscillations around a mean rise velocity are observed. The simulated diameters are contained in Tables B4–B6.

This section will be organized as follows: the shape regimes of droplets in the three test systems will be identified and compared to the graphical correlation given by Grace et al. (1976). For a closer investigation of the deformation, the transient aspect ratio of the droplets will be investigated. Finally, the terminal velocities for the three test systems are presented and compared to experimental data.

4.1. Shape deformation and aspect ratio

Shape deformation and oscillation are important interfacial effects with significant impact on fluid dynamics. Hence, a numerical method should be capable of simulating deformations accurately. Fig. 10 shows contour plots of toluene droplets with d_P=4.4 mm simulated with Navier in comparison to photographs of real toluene droplets with the same size at arbitrary times. The different stages in shape deformation are well represented by the simulations and demonstrate the capability of the code to capture the free interface.

Fig. 11 contains drop contours at terminal velocity for different droplet diameters for the systems toluene/water, n-butyl acetate/water and n-butanol/water, from the left column to the right. The first row shows droplets with an equivalent diameter of d_P=1.0 mm, the second row displays those droplets which attain the maximum terminal velocity, and in the third row the largest droplet diameters performed in the simulations are drawn.

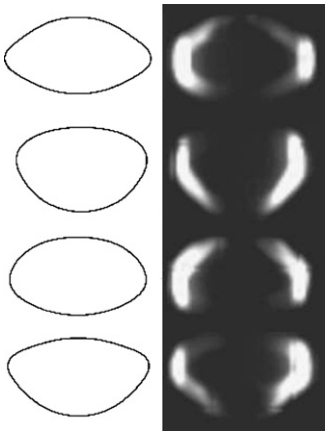

Fig. 10. Simulated contour plots of 4.4 mm toluene droplets with different aspect ratio in comparison to photographs of real toluene droplets.

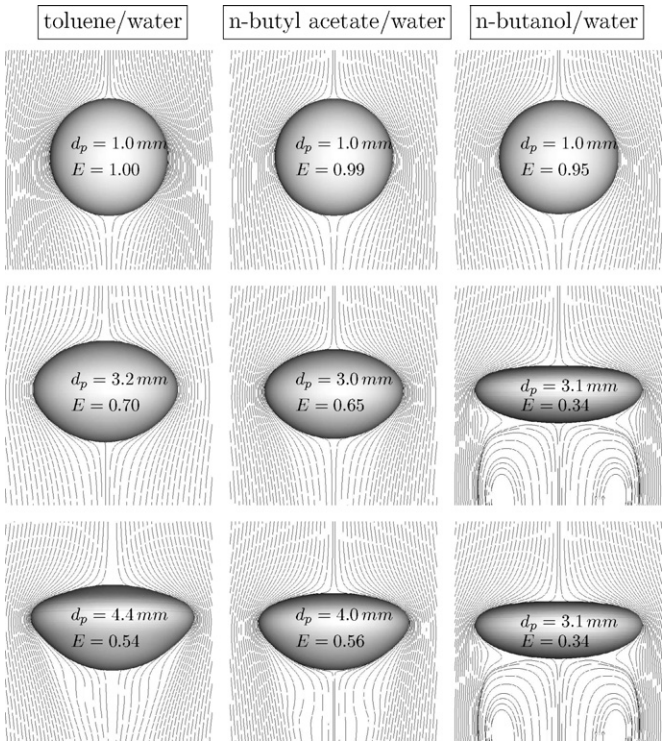

Fig. 11. Computational results: droplet deformation and aspect ratios with velocity streamlines of the three test systems in different regimes. First row: spherical regime with d_P=1.0 mm, middle row: droplets at maximum velocity, last row: the largest diameter simulated with NAVIER in this study.

The 1.0 mm droplets can be regarded as spherical, following the definition given by Michaelides (2006) whereby the lengths of the two principal axes are within 5%, i.e. the aspect ratio $E \geq 0.95$, which is the case for all three droplets. Due to the high interfacial tension in the toluene/water system, $E=1$ for small droplets.

In the second row, shapes of droplets moving at maximum velocity are compared. The maximum velocity occurs nearly at equal droplet diameters: for toluene: 3.2 mm, *n*-butyl acetate: 3.0 mm, and for *n*-butanol: 3.1 mm (this coincides with the largest simulated diameter). The higher the interfacial tension, the higher the aspect ratio at which maximum velocity is attained. Toluene droplets are the fastest with an aspect ratio of $E=0.7$, whereas *n*-butyl acetate droplets reach their maximum at a relatively strong deformation with $E=0.65$, and *n*-butanol droplets for an even lower aspect ratio at $E=0.34$. Comparisons to shapes provided by Bertakis et al. (2010) show good agreement for the *n*-butanol system (for the 3.0 mm droplet with $E_{Bertakis} \approx 0.4$, $E_{Navier} = 0.36$).

The third row in Fig. 11 shows the largest droplet diameter simulated in this study for the respective system. Especially for the toluene droplet, no fore-and-aft symmetry can be observed at a diameter d_P=4.4 mm. The *n*-butanol droplet has clearly less deviation of a fore-and-aft symmetric shape and exhibits the lowest aspect ratio in this study ($E=0.34$).

The *n*-butanol drop with d_p=3.1 mm is the only droplet in Fig. 11 exhibiting a vortex in the wake of the droplet. Vortices appear in the wake of *n*-butanol droplets for diameters larger than 2.0 mm. In the other systems no vortices were observed at any diameter.

A general observation for all droplet diameters is that the lower the interfacial tension is, the more oblate the droplet becomes (prolate droplets were never observed for any diameter simulated in this study, see Table B7).

In Fig. 12, the transient drop rise velocities (left ordinate) and aspect ratios (right ordinate) for the droplet diameters shown in Fig. 11 are displayed. Initially the droplet has spherical shape, and eventually deforms during its rise through the ambient liquid. For 1.0 mm droplets, terminal velocity is attained in no more than 0.25 s in all cases and deformation is negligible. Generally, the higher the viscosity ratio, the slower are the spherical droplets.

The droplets at maximum velocity show stable behavior for the toluene/water and the *n*-butyl acetate/water systems. The *n*-butanol system behaves slightly differently from the two systems with higher interfacial tension. During acceleration stage, slight oscillations appear in the *n*-butanol/water system, presumably due to the low interfacial tension (this behavior is observed for butanol droplets with $d_P > 2.6$ mm), see Fig. 12. The oscillations are damped during the rise and finally vanish when the droplets reach terminal velocity. Smaller droplet diameters in the *n*-butanol system, and droplets in the other two test systems accelerate monotonously.

The curves for the largest droplet diameter simulated show frequent oscillations around a mean value with increasing amplitude in the toluene and the *n*-butyl acetate systems. These oscillations can be attributed to numerical effects, since experimental oscillations in velocity are of significantly lower frequency. For longer times the amplitude of the aspect ratio oscillation increases, and the simulations become unstable due to strong mesh deformations and finally the simulation breaks down. Unfortunately, this has to be expected for the currently implemented mesh moving method. Eventually this drawback of the numerical method could be avoided by an elaborate remeshing-routine, or stronger grid smoothing. However, the present study focuses on the diameter range until onset of oscillation.

Fig. 13 shows the simulated aspect ratio *E* as a function of Eötvös number *Eo* for the three test systems (see also Table B7). For comparison, a correlation given by Wellek et al. (1966) for contaminated systems is also plotted in Fig. 13:

$$E = \frac{1}{(1+0.163Eo^{0.757})} \quad \text{with } Eo < 40; Mo \leq 10^{-6} \tag{11}$$

Generally the simulations capture the decreasing aspect ratio *E* for increasing Eötvös number in each test system. Droplets in pure systems are more deformed than in the corresponding contaminated system. Hence the correlation by Wellek et al. (1966) is not suitable to describe uncontaminated systems used in this study, as reported as well by Clift et al. (1978). Reflecting the findings of Clift et al. (1978, Chapter 7), deformation also depends on the Morton number, in a way that higher Morton numbers give rise to less deformation at the same Eötvös number. The data can be represented by the following simple correlation:

$$E = e^{-aEo^b}. \tag{12}$$

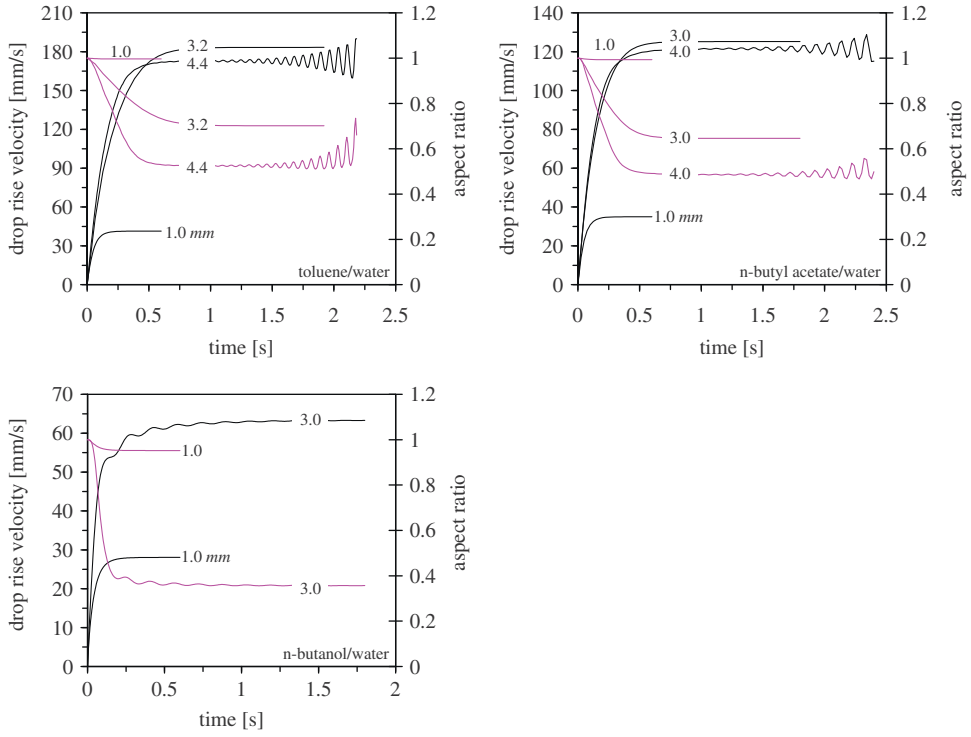

Fig. 12. Simulated drop rise velocity (increasing curves) and aspect ratio (decreasing curves) as a function of time for the three test systems at different diameters. Upper left: toluene/water, upper right: *n*-butyl acetate/water, lower left: *n*-butanol/water.

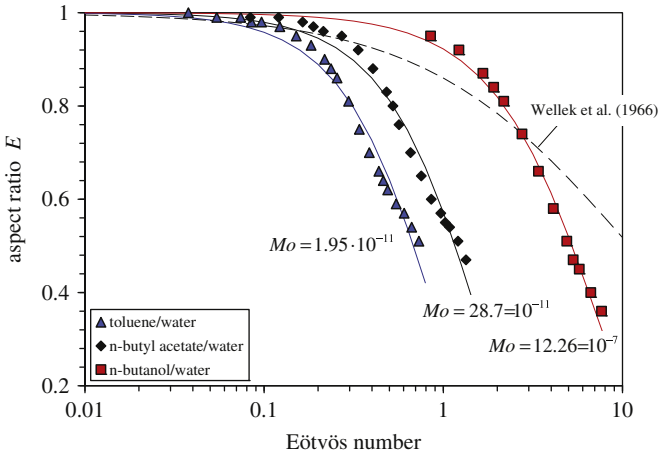

Fig. 13. Simulated aspect ratio for the different systems in comparison to the correlation for contaminated systems by Wellek et al. (1966).

The parameters a and b have been obtained by regression analysis and are listed in Table 3, the corresponding curves are plotted in Fig. 13.

Shape deformation data for validation is available in the famous graphical correlation presented by Grace et al. (1976) for a wide range of Eötvös and Morton numbers. The simulation results are plotted in the graphical correlation in Fig. 14. The plot shows the Reynolds number versus Eötvös number for different Morton numbers for the three test systems (see Table 1). The correlation holds for moderate density and viscosity ratios. Droplet viscosity μ_d is not considered in any of the three dimensionless numbers, but μ_d may be significant in purified systems (Clift et al., 1978). The plot is suitable for a first approximation, but nevertheless, more accurate correlations exist in many cases.

Given the explanation in Clift et al. (1978) that in Fig. 14 "the boundaries between the principal shape regimes are somewhat

Table 3
Parameters a and b in Eq. (12) for the three test systems.

	Toluene/water	*n*-Butyl acetate/water	*n*-Butanol/water
a	1.209	0.559	0.081
b	1.449	1.427	1.299

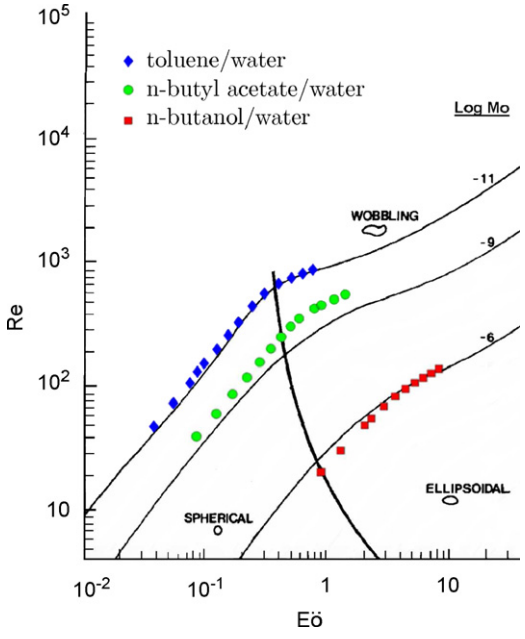

Fig. 14. Simulated Reynolds numbers at steady state as a function of Eötvös number for different Morton numbers (graphical correlation by Grace et al., 1976). Comparison of simulated data for the three test systems with correlation predictions.

arbitrary", we find a good agreement especially for the toluene/water system. The data follow accurately the respective curve for the Morton number. The Morton number for the *n*-butyl acetate system is $Mo \approx 3 \times 10^{-10}$. The parallelism as obtained in the toluene/water system does not occur. The *n*-butanol/water system is well represented by the correlation for bigger droplets. For smaller droplets, the Reynolds number obtained by the simulations (and in the experiments, compare with Table B4) is lower than predicted by the graphical plot.

The transition from spherical to ellipsoidal regime appears in the simulations for droplets > 1.0 mm (see Table B7), this is perfectly predicted by the correlation. For higher Morton numbers as in the case for the toluene or *n*-butyl acetate system, the correlation suggests that there is a transition from spherical to wobbling regime, which is not true in reality. Droplets deform first with no oscillations, irregular shape wobbling sets in for larger droplets.

4.2. Terminal drop rise velocity

The simulated terminal velocities as a function of droplet diameter are plotted in Figs. 15–17 for each test system. The corresponding values can be found in Tables B4–B6. The fit of experimental data on the basis of Henschke's model (dotted curve) is based on the characteristic mean values u_{cha} (in the diameter range 2.2…3.0 mm in the toluene/water system, where velocity oscillations and bifurcation occur, the maximum values were used) using the parameters in Table 2. In each figure, the three regimes for spherical, deformable and oscillating droplets are separated by vertical lines. The left line is based on our simulation results where $E=0.95$. Besides the Klee and Treybal correlation (chain line) indicating here the onset of oscillation, simulation results were taken into account (full line on the right in each figure).

For non-oscillating droplets, the terminal velocity in the simulations is evaluated after steady state is reached. For shape oscillating droplets, no constant terminal velocity is attained, the rise velocity rather oscillates around a mean velocity. This mean rise velocity $u_{t_{Navier}}$ is obtained by time-averaging the rise velocity over a time span of three shape oscillations.

Fig. 15 shows the results for the toluene/water system. The agreement is excellent over the whole diameter range capturing the specifics in all regimes with a mean deviation of 2.5% based on the experimental maximum values and 4.6% based on the characteristic mean values (without bifurcation data). The maximum velocity is obtained for 3.2 mm droplets in the simulations as well

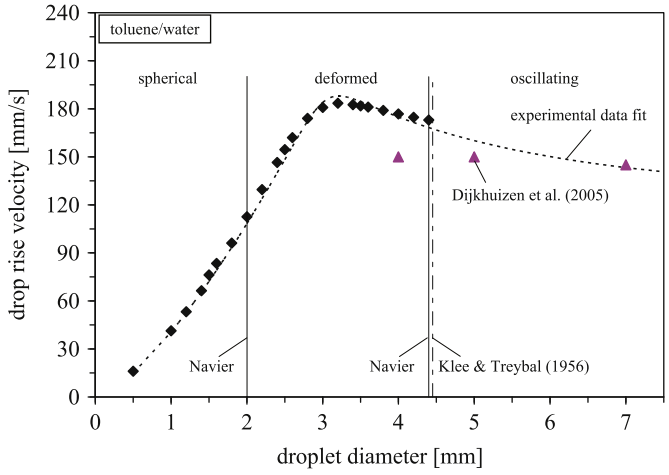

Fig. 15. Simulated drop rise velocities (rhombii) of toluene droplets in water as a function of droplet diameter compared to experimental (dotted curve) (Wegener et al., 2010) and simulation (triangles) (Dijkhuizen et al., 2005) data. $\vartheta = 25$ °C.

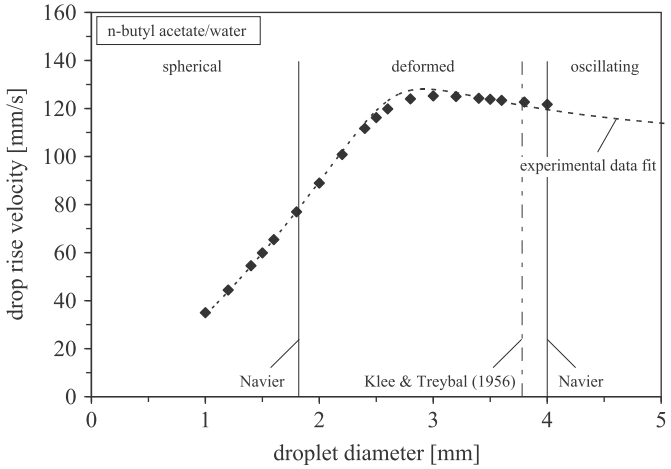

Fig. 16. Simulated drop rise velocities (rhombii) of *n*-butyl acetate droplets in water as a function of droplet diameter compared to own experimental data (dotted curve). $\vartheta = 25$ °C.

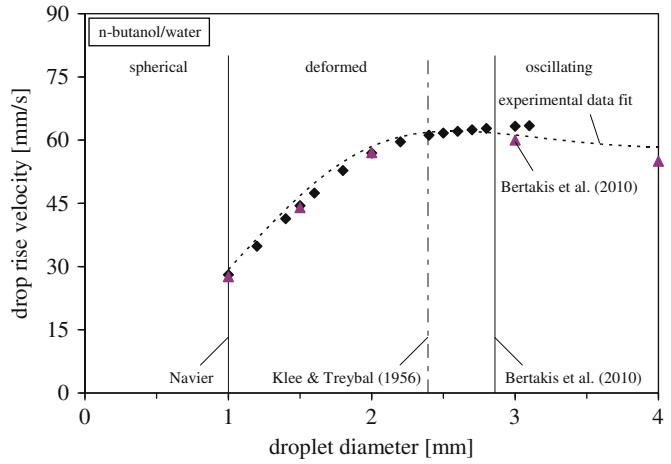

Fig. 17. Simulated drop rise velocities (rhombii) of *n*-butanol droplets in water as a function of droplet diameter compared to experimental (dotted curve) and simulation (triangles) data (both Bertakis et al., 2010). $\vartheta = 20$ °C.

as in the experiments. Another point of interest is the onset of oscillations. In our simulations, we define a droplet to be shape oscillating if its aspect ratio *E* varies more than 2% after the mean rise velocity $u_{t_{Navier}}$ has been reached. In the simulations shape oscillations were observed for $d_P = 4.4$ mm. This practically coincides with the critical diameter $d_{cr} = 4.45$ mm predicted by the Klee and Treybal correlation in Eq. (1). It is interesting to notice that compared to the experimental correlation in Fig. 3, the simulations match the maximum values of the bifurcation data. The presented simulations for toluene/water comprise the diameter range $d_P \in [0.5 \ldots 4.4\ \text{mm}]$. The upper limit of the simulations is due to the strong deformations that can be captured by the sharp interface representation only up to a certain amount. In Fig. 15, simulation data for droplets published by Dijkhuizen et al. (2005) are given for comparison. The 7 mm oscillating droplet matches the experimental data fit curve (1% deviation for the mean value), whereas the velocity for the 5 mm and especially for the 4 mm droplet (non-oscillating deformed droplets) is significantly too low compared to measurements and our own simulations (6% and 14% deviation, respectively).

Similar agreement to the results of *n*-butyl acetate/water was found. A plot is given in Fig. 16 with the corresponding data in Table B5. The mean deviation is in a similar range: 3.0% based on the experimental maximum values and 4.7% based on the

characteristic mean values. The diameter at maximum velocity determined in the simulations is 3.0 mm which is in agreement with the experimental data (u_{cha}). Note that the maximum is less pronounced than for the toluene system with higher interfacial tension. The onset of oscillations according to the above described criteria is found at a diameter of 4.0 mm, which is less accurate than in the toluene system compared to the value found in the experiments (d_{cr}=3.78 mm). The largest simulated diameter with NAVIER in this test system was 4.0 mm.

For the system *n*-butanol/water the simulated diameters span the range $d_P \in [1.0 \ldots 3.1\ \text{mm}]$ (Fig. 17). Due to the low interfacial tension the droplets develop the smallest aspect ratios, both as an absolute value and in comparison to the other test systems for droplets of the same diameter. Our own simulations are compared to the data fit based on the experimental values presented by Bertakis et al. (2010) and their simulation data (see Table B6). In the experimental data published by Bertakis et al. (2010) the maximum is reached at d_P=2.48 mm, accordingly, for the data fit ($u_{t_{Henschke}}$) the maximum is found at 2.5 mm, whereas the simulations of Bertakis et al. reach the maximum at 3.0 mm just slightly below the simulations with NAVIER, with 3.1 mm. In general, the agreement between our simulations with those by Bertakis et al. is excellent.

Following Bertakis et al., the onset of oscillation is at about 2.86 mm, compared to the other two systems, the maximum peak is hardly visible which has to be attributed to the low interfacial tension. The correlation of Klee and Treybal obviously gives a wrong result.

5. Conclusions

A detailed numerical study of drop rise behavior in three standard test systems used for liquid/liquid extraction (toluene/water, *n*-butyl acetate/water, *n*-butanol/water, representing high, medium and low interfacial tension, respectively) has been accomplished using the academic FEM code NAVIER. The code comprises a sharp interface representation and a variational formulation of the curvature providing an effective method for a consistent, very exact description of discrete surface stresses.

Experimental terminal drop rise velocities were compared with correlations available in the literature. In all experiments, special care was taken to keep the system clean from contaminants. For the high and medium interfacial tension systems very good agreement with the drag coefficient correlation proposed by Hamielec et al. (1963) in the spherical regime nearly up to the droplet diameter at maximum velocity can be stated. The correlations by Thorsen et al. (1968) and Harper (1972) show fair agreement in the oscillatory regime. Only the transition region between the spherical and oscillatory regime is not covered by the models. A model proposed by Henschke (2004) is applied to represent the experimental values by one single curve which is continuous over the whole diameter range. The model parameters have been fitted to experimental data. In the *n*-butanol system, experimental data published by Bertakis et al. (2010) has been used for the comparisons. Agreement with literature correlations is poor, except for correlation (2) given by Hamielec et al. (1963). This is not due to erroneous measurements (agreement with simulations is excellent), but probably due to the fact that *n*-butanol/water has a very low interfacial tension in combination with a relatively high absolute droplet viscosity and a higher viscosity ratio which makes literature correlations inapplicable in this case.

Simulated terminal drop rise velocities were compared over a wide range of droplet diameters with experimental data available in literature (toluene/water: Wegener et al., 2010, *n*-butanol/water: Bertakis et al., 2010) or with experiments made for this study (*n*-butyl acetate/water), and with numerical data presented by Dijkhuizen et al. (2005) (toluene/water) and Bertakis et al. (2010) (*n*-butanol/water). Additionally, the simulated transient and steady state aspect ratio is evaluated. Droplet shape is compared with the graphical correlation by Grace et al. (1976).

Simulations captured the decreasing aspect ratio for increasing Eötvös numbers. The fact, that for a given Eötvös number the aspect ratio is higher for systems with higher Morton number was also mirrored in the simulations. The aspect ratio correlation proposed by Wellek et al. (1966) is only valid for contaminated systems and does not coincide with the present data, thus, a simple empirical correlation is proposed to describe the present results. The general findings agree with results collected by Clift et al. (1978). Shape prediction using the famous graphical correlation by Grace et al. (1976) should be applied with caution, nevertheless, it can be used for a rough estimation for the systems used here.

Simulated terminal drop rise velocities agree in an excellent manner with experimental findings for all three systems. The mean deviation is below 5%. Maximum velocity is correctly predicted, and the fact that the maximum is less pronounced in low interfacial systems is captured by our simulations. Problems with the code NAVIER occur for strongly deformed droplets in the oscillatory regime. This is a drawback of the chosen method, since high interface velocities, Eq. (7), might lead to severe mesh distortion, resulting in a less-quality mesh, or even distort the mesh completely by flipping one node across the opposite edge, thus making the triangulation non-admissible. A possible remedy of this problem is the implementation of a remeshing routine, or the combination of very small time steps and an elaborate grid-smoothing routine.

However the objective of our future work will be to satisfyingly simulate mass transfer at high Peclet numbers in the present setting.

Notation

a,b	coefficients
C_D	drag coefficient
d_P	droplet diameter, m
E	aspect ratio, ratio of polar to equatorial length
g	gravitational acceleration, m/s^2
I	identity matrix
p	pressure, kg/ms^2
$p_1 \ldots p_5$	parameters in the Henschke model
t	time, s
T	Newtonian stress tensor N/m^2
$\mathbf{u}$	velocity, (m/s)^3
u_t	terminal velocity, m/s
V_Γ	interface velocity, (m/s)^3
V	drop volume, m^3
$\mathbf{x}_B$	barycenter of droplet

Dimensionless numbers

Ar	Archimedes number, $d_P^3 g \rho_c \Delta\rho / \mu_c^2$
Eo	Eötvös number, $g \Delta\rho d_P^2 / \sigma$
Mo	Morton number, $g \mu_c^4 \Delta\rho / \rho_c^2 \sigma^3$
Re	Reynolds number $u_t d_P \rho_c / \mu_c$
We	Weber number, $u_t^2 d_P \rho_c / \sigma$

Greek letters

Γ	interface
ϑ	temperature, °C
κ	curvature, 1/m
μ	dynamic viscosity, Pa s
μ^*	viscosity ratio μ_d / μ_c
ν	unit normal
ρ	density, kg/m^3
ρ^*	density ratio ρ_d / ρ_c
$\Delta\rho$	density difference, kg/m^3
σ	interfacial tension, N/m

Φ	coordinate transformation from reference to drop coordinate system
Ω	bulk phase

Subscripts

0	initial
c	continuous phase
circ	circulating
cr	critical
cha	characteristic
d	dispersed phase, droplet
def	deformed
HR	Hadamard and Rybczynski
i	inertia
max	maximum
os	oscillating
rigid	rigid particle
sph	spherical
t	terminal
tr	travel
w	water

Acknowledgement

The authors like to acknowledge the German Research Foundation (DFG) for financial support.

Appendix A

A.1. Terminal velocity correlation by Grace et al.

According to their publication Grace et al. (1976), for contaminated systems the terminal velocity can be calculated with the following equations:

$$u_t = \frac{\mu_c}{\rho_c d_P} Mo^{-0.149}(J-0.857) \tag{A.1}$$

with

$$J = 0.94H^{0.757} \quad (2 < H \leq 59.3) \tag{A.2}$$

and

$$J = 3.42H^{0.441} \quad (H > 59.3) \tag{A.3}$$

H is defined as follows:

$$H = \frac{4}{3} EoMo^{-0.149}\left(\frac{\mu_c}{\mu_w}\right)^{-0.14} \quad \text{with } \mu_w = 0.9 \text{ m Pa s} \tag{A.4}$$

A.2. Henschke model to calculate the terminal drop rise velocity

The expression for the terminal velocity according to the Henschke model (Bertakis et al., 2010; Henschke, 2004) is composed of the velocities of spherical, deformed and oscillating droplets, u_{sph}, u_{def} and u_{os}, and reads

$$u_t = \frac{u_{def,os} u_{sph}}{(u_{def,os}^{p_3} + u_{sph}^{p_3})^{1/p_3}} \tag{A.5}$$

with the parameter p_3 (the physical meaning of the parameters is explained in detail in Bertakis et al., 2010). $u_{def,os}$ is a combination of the two velocities u_{def} and u_{os}:

$$u_{def,os} = (u_{def}^{p_5} + u_{os}^{p_5})^{1/p_5} \tag{A.6}$$

with $u_{def} = (d_P g \Delta\rho / 2\rho_c)^{1/2}$ and $u_{os} = (2p_2\sigma/d_P\rho_c)^{1/2}$. The terminal velocity of spherical droplets u_{sph} reads

$$u_{sph} = \frac{\mu_c Re_{sph}}{d_P \rho_c} \tag{A.7}$$

with $Re_{sph} = (1-f)Re_{rigid} + fRe_{circ}$ where $f = 2(K_{HR}-1)$, K_{HR} being the corrected Hadamard–Rybczynski factor:

$$K_{HR} = \frac{3(\mu_c + \mu_d/\beta)}{2\mu_c + 3\mu_d/\beta} \tag{A.8}$$

with the correction $\beta = 1 - 1/(1+(d_P/p_1)^{p_4})$. In order to calculate the two Reynolds numbers Re_{rigid} and Re_{circ}, the Archimedes number

$$Ar = \frac{d_P^3 g \rho_c \Delta\rho}{\mu_c^2} \tag{A.9}$$

is required:

$$Re_{circ} = \frac{Ar}{12(0.065Ar+1)^{1/6}} \tag{A.10}$$

and

$$Re_{rigid} = \left(\frac{4Ar}{3C_D}\right)^{1/2} \tag{A.11}$$

with the drag coefficient $C_D = 432/Ar + 20/Ar^{1/3} + 0.51Ar^{1/3}/(Ar^{1/3} + 140)$.

Appendix B. Auxiliary tables

See Tables B4–B7.

Table B4
Drop rise velocities in the toluene/water system. The first and second column (u_{cha} and u_{max}) contain experimental data by Wegener et al. (2010). $u_{t_{Navier}}$ and $u_{t_{Navier},max}$ are results from simulations with Navier (this study). The two columns $u_{t_{Hamielec}}$ and $u_{t_{Henschke}}$ are correlations given by Hamielec et al. (1963) and Henschke (2004), respectively. Velocities $u_{t_{Navier}}$ marked with an asterisk '*' show oscillations. The values are calculated by time averaging the velocities over three oscillations.

d_P (mm)	u_{cha} (mm/s)	u_{max} (mm/s)	$u_{t_{Navier}}$ (mm/s)	$u_{t_{Navier},max}$ (mm/s)	$u_{t_{Hamielec}}$ (mm/s)	$u_{t_{Henschke}}$ (mm/s)
0.5	–	–	16.04	–	15.58	14.98
1.0	35.67	40.17	41.35	–	40.58	41.09
1.2	46.26	50.12	53.23	–	52.20	53.22
1.4	58.79	62.22	66.34	–	64.58	66.18
1.5	67.43	70.53	76.19	–	71.04	72.95
1.6	76.08	78.85	83.38	–	77.66	79.90
1.8	91.81	94.49	96.14	–	91.38	94.32
2.0	109.96	111.16	112.57	–	105.69	109.38
2.2	122.52	128.95	129.58	–	120.56	125.03
2.4	108.20	145.20	146.49	–	135.95	141.14
2.5	108.17	154.43	154.53	–	143.83	149.29
2.6	108.91	161.04	161.99	–	151.84	157.38
2.8	112.01	173.60	174.03	–	168.20	172.50
3.0	135.76	183.31	180.85	–	185.01	183.55
3.2	186.39	186.74	183.44	–	202.26	187.94
3.4	185.42	186.36	182.52	–	219.92	187.21
3.5	184.64	186.31	181.82	–	–	185.93
3.6	183.75	185.00	181.09	–	–	184.40
3.8	180.43	182.16	178.98	–	–	181.10
4.0	178.25	179.78	176.78	–	–	177.86
4.2	176.19	177.97	174.68	–	–	174.83
4.4	173.27	176.13	173.00*	186.19	–	172.04
4.5	171.69	175.14	–	–	–	170.73
4.6	163.54	174.56	–	–	–	169.47
4.8	156.88	171.59	–	–	–	167.11
5.0	152.92	173.28	–	–	–	164.95
5.2	146.14	173.18	–	–	–	162.95
5.4	152.70	170.52	–	–	–	161.12
5.6	151.45	168.88	–	–	–	159.42
5.8	151.04	164.77	–	–	–	157.86
6.0	151.25	163.21	–	–	–	156.41
6.2	149.53	159.26	–	–	–	155.07
6.4	148.10	157.82	–	–	–	153.83
6.6	151.28	159.11	–	–	–	152.68
6.8	144.29	153.83	–	–	–	151.62
7.0	148.34	156.14	–	–	–	150.64

Table B5
Drop rise velocities in the *n*-butyl acetate/water system. The first and second column (u_{cha} and u_{max}) contain experimental data (this study). $u_{t_{Navier}}$ and $u_{t_{Navier},max}$ are results from the simulations with Navier. The two columns $u_{t_{Hamielec}}$ and $u_{t_{Henschke}}$ are correlations given by Hamielec et al. (1963) and Henschke (2004), respectively. Velocities $u_{t_{Navier}}$ marked with an asterisk '*' show oscillations. The values are calculated by time averaging the velocities over three oscillations.

d_P (mm)	u_{cha} (mm/s)	u_{max} (mm/s)	$u_{t_{Navier}}$ (mm/s)	$u_{t_{Navier},max}$ (mm/s)	$u_{t_{Hamielec}}$ (mm/s)	$u_{t_{Henschke}}$ (mm/s)
1.0	30.80	32.50	34.98	–	35.58	34.85
1.2	41.40	46.50	44.39	–	45.76	44.96
1.4	52.20	56.00	54.52	–	56.62	55.77
1.5	57.50	61.40	59.87	–	62.28	61.42
1.6	64.80	68.80	65.40	–	68.09	67.22
1.8	77.17	80.30	76.95	–	80.11	79.26
2.0	91.07	95.52	88.93	–	92.66	91.80
2.2	104.31	109.81	100.85	–	105.69	104.55
2.4	115.64	119.52	111.70	–	119.19	116.46
2.5	120.75	125.74	116.20	–	126.10	121.40
2.6	121.94	124.31	119.80	–	133.12	125.21
2.8	126.32	130.58	124.00	–	147.46	129.02
3.0	127.30	129.86	125.22	–	162.20	129.26
3.2	125.86	130.14	124.98	–	–	128.09
3.4	125.24	127.57	124.24	–	–	126.58
3.5	125.06	128.24	123.82	–	–	125.83
3.6	124.53	128.00	123.40	–	–	125.10
3.8	123.55	127.90	122.29	–	–	123.75
4.0	119.00	125.80	121.70*	129.11	–	122.54
4.2	117.25	124.6	–	–	–	121.48
4.4	116.50	124.00	–	–	–	120.54
4.5	116.48	122.80	–	–	–	120.12

Table B6
Drop rise velocities in the *n*-butanol/water system. The first column ($u_{t_{exp,Bertakis}}$) contains experimental data by Bertakis et al. (2010). The second and third column are simulation results from Bertakis et al. (2010) ($u_{t_{sim,Bertakis}}$ and from this study ($u_{t_{Navier}}$). The last column $u_{t_{Henschke}}$ is a correlation given by Henschke (2004).

d_P (mm)	$u_{t_{exp,Bertakis}}$ (mm/s)	$u_{t_{sim,Bertakis}}$ (mm/s)	$u_{t_{Navier}}$ (mm/s)	$u_{t_{Henschke}}$ (mm/s)
1.0	–	27.6	28.07	29.26
1.2	–	–	34.83	36.61
1.4	–	–	41.35	43.58
1.5	–	44	44.46	46.80
1.56	45	–	46.13	48.61
1.6	–	–	47.43	–
1.79	52	–	52.40	54.59
1.8	–	–	52.77	54.81
2.0	–	57	56.92	58.49
2.12	59	–	58.62	60.02
2.2	–	–	59.62	60.79
2.26	61	–	60.01	61.23
2.4	–	–	61.17	61.91
2.48	63	–	61.52	62.10
2.5	–	–	61.68	62.13
2.6	–	–	62.10	–
2.7	–	–	62.46	–
2.8	–	–	62.78	–
3.0	–	60	63.30	61.21
3.06	62	–	63.36	60.99
3.1	–	–	63.41	60.99
3.48	58	–	–	59.42
4.0	–	55	–	58.39

Table B7
Aspect ratios from simulations with Navier (this study) in the three test systems.

d_P (mm)	$E=d_{vert}/d_{hor}$, toluene/water	$E=d_{vert}/d_{hor}$, *n*-butyl acetate/water	$E=d_{vert}/d_{hor}$, *n*-butanol/water
1.0	1.00	0.99	0.95
1.2	0.99	0.99	0.92
1.4	0.99	0.98	0.87
1.5	0.98	0.97	0.84
1.6	0.98	0.96	0.81
1.8	0.97	0.95	0.74
2.0	0.95	0.92	0.66
2.2	0.93	0.88	0.58
2.4	0.90	0.83	0.51
2.5	0.88	0.80	0.47
2.6	0.86	0.76	0.45
2.8	0.81	0.70	0.40
3.0	0.75	0.65	0.36
3.1	–	–	0.34
3.2	0.70	0.60	–
3.4	0.66	0.57	–
3.5	0.64	0.55	–
3.6	0.62	0.54	–
3.8	0.59	0.51	–
4.0	0.57	0.47–0.56	–
4.2	0.54	–	–
4.4	0.51–0.74	–	–

References

Bänsch, E., 2001. Finite element discretization of the Navier–Stokes equations with a free capillary surface. Numerical Mathematics 88, 203–235.

Bänsch, E., Berg, C.P., Ohlhoff, A., 2004a. Uniaxial, extensional flows in liquid bridges. Journal of Fluid Mechanics 521, 353–379.

Bänsch, E., Davis, D., Langmach, H., Miller, W., Rehse, U., Reinhardt, G., Uhle, M., 2004b. Axisymmetric and 3D calculations of melt flow during VCz growth. Journal of Crystal Growth 266 (1–3), 60–66.

Bänsch, E., Hauer, F., Lakkis, O., Li, B., Voigt, A., 2004c. Finite element method for epitaxial growth with attachment–detachment kinetics. Journal of Computational Physics 194 (2), 409–434.

Bänsch, E., Schmidt, A., 2000. Simulation of dendritic crystal growth with thermal convection. Interfaces and Free Boundaries 2, 95–115.

Bertakis, E., Groß, S., Grande, J., Fortmeier, O., Reusken, A., Pfennig, A., 2010. Validated simulation of droplet sedimentation with finite-element and level-set methods. Chemical Engineering Science 65 (6), 2037–2051.

Clift, R., Grace, J.R., Weber, M.E., 1978. Bubbles, Drops, and Particles. Academic Press, New York.

Deshpande, K.B., Zimmerman, W.B., 2006. Simulation of interfacial mass transfer by droplet dynamics using the level set method. Chemical Engineering Science 61 (19), 6486–6498.

Dijkhuizen, W., van Sint Annaland, M., Kuipers, H., 2005. Numerical investigation of closures for interface forces in dispersed flows using a 3d front tracking model. In: Proceedings of the 4th International Conference on CFD in Oil and Gas, Metallurgical & Process Industries, SINTEF, Trondheim, Norway.

Dziuk, G., 1988. Finite elements for the Beltrami operator on arbitrary surfaces. In: Springer Lecture Notes in Mathematics, vol. 1357, pp. 142–155.

Feng, Z.-G., Michaelides, E.E., 2001. Drag coefficients of viscous spheres at intermediate and high Reynolds numbers. Journal of Fluids Engineering 123 (4), 841–849.

Grace, J.R., Wairegi, T., Nguyen, T.H., 1976. Shapes and velocities of single drops and bubbles moving freely through immiscible liquids. Transactions of the Institution of Chemical Engineers 54, 167–173.

Groß, S., Reichelt, V., Reusken, A., 2006. A finite element based level set method for two-phase incompressible flows. Computation and Visualization in Science 9 (4), 239–257.

Hadamard, J.S., 1911. Mouvement permanent lent d'une sphère liquide et visqueuse dans un liquide visqueux. Comptes Rendus de l'Académie des Sciences Paris 152, 1735–1743.

Hamielec, A.E., Storey, S.H., Whitehead, J.M., 1963. Viscous flow around fluid spheres at intermediate Reynolds-numbers. Canadian Journal of Chemical Engineering 12, 246–251.

Harper, J. F., 1972. The motion of bubbles and drops through liquids. In: Advances in Applied Mechanics, vol. 12. Elsevier, pp. 59–129.

Henschke, M., 2004. Auslegung pulsierter Siebboden-Kolonnen. Berichte aus der Verfahrenstechnik. Shaker Verlag Aachen, Habilitation Thesis.

Hu, S., Kintner, R.C., 1955. The fall of single liquid drops through water. AIChE Journal 1 (1), 42–48.

Klee, A.J., Treybal, R.E., 1956. Rate of rise or fall of liquid drops. AIChE Journal 2 (4), 444–447.

Krishna, P.M., Venkateswarlu, D., Narasimhamurty, G.S.R., 1959. Fall of liquid drops in water. Terminal velocities. Journal of Chemical & Engineering Data 4 (4), 336–340.

Loth, E., 2008. Quasi-steady shape and drag of deformable bubbles and drops. International Journal of Multiphase Flow 34 (6), 523–546.

Maxey, M.R., Riley, J.J., 1983. Equation of motion for a small rigid sphere in a nonuniform flow. Physics of Fluids 26 (4), 883–889.

Michaelides, E.E., 2006. Particles Bubbles & Drops. World Scientific Publishing, Singapore.

Misek, T., Berger, R., Schröter, J., 1985. Standard test systems for liquid extraction. Institute of Chemical Engineers, EFCE Publication Series 46.

Petera, J., Weatherley, L.R., 2001. Modelling of mass transfer from falling droplets. Chemical Engineering Science 56 (16), 4929–4947.
Prignitz, R., Bänsch, E., 2010. Numerical simulation of suspension induced rheology. Kybernetika 46 (2), 281–293.
Rivkind, V.Y., Ryskin, G.M., 1976. Flow structure in motion of a spherical drop in a fluid medium at intermediate Reynolds numbers. Journal of Fluid Dynamics 11 (1), 5–12.
Rivkind, V.Y., Ryskin, G.M., Fishbein, G.A., 1976. Flow around a spherical drop at intermediate Reynolds numbers. Journal of Applied Mathematics and Mechanics 40 (4), 687–691.
Rybczynski, W., 1911. Über die fortschreitende Bewegung einer flüssigen Kugel in einem zähen Medium. Bulletin international de l'Académie des Sciences de Cracovie, Classe des Sciences Mathématiques et Naturelles. Série A, Sciences Mathématiques, 40–46.
Saboni, A., Alexandrova, S., 2002. Numerical study of the drag on a fluid sphere. AIChE Journal 48 (12), 2992–2994.
Thorsen, G., Stordalen, R.M., Terjesen, S.G., 1968. On the terminal velocity of circulating and oscillating liquid drops. Chemical Engineering Science 23 (5), 413–426.
Waheed, M.A., Henschke, M., Pfennig, A., 2004. Simulating sedimentation of liquid drops. International Journal for Numerical Methods in Engineering 59 (14), 1821–1837.
Wang, J., Lu, P., Wang, Z., Yang, C., Mao, Z.-S., 2008. Numerical simulation of unsteady mass transfer by the level set method. Chemical Engineering Science 63 (12), 3141–3151.
Watanabe, T., Ebihara, K., 2003. Numerical simulation of coalescence and breakup of rising droplets. Computers & Fluids 32 (6), 823–834.
Wegener, M., 2009. Der Einfluss der konzentrationsinduzierten Marangonikonvektion auf den instationären Impuls- und Stofftransport an Einzeltropfen. Ph.D. Thesis, Chair of Chemical & Process Engineering, TU Berlin, Germany. 〈URL: http://opus.kobv.de/tuberlin/volltexte/2009/2507/〉.
Wegener, M., Eppinger, T., Bäumler, K., Kraume, M., Paschedag, A.R., Bänsch, E., 2009. Transient rise velocity and mass transfer of a single drop with interfacial instabilities—numerical investigations. Chemical Engineering Science 64 (23), 4835–4845.
Wegener, M., Kraume, M., Paschedag, A.R., 2010. Terminal and transient drop rise velocity of single toluene droplets in water. AIChE Journal 56 (1), 2–10.
Weking, H., Weigand, B., 2008. Numerical investigation on the rise behaviour of single gaseous bubbles in quiescent liquids. In: Proceedings of the 6th International Conference on CFD in Oil and Gas, Metallurgical an Process Industries, SINTEF.
Wellek, R.M., Agrawal, A.K., Skelland, A.H.P., 1966. Shape of liquid drops moving in liquid media. AIChE Journal 12 (5), 854–862.
Winnikow, S., Chao, B.T., 1966. Droplet motion in purified systems. Physics of Fluids 9 (1), 50–61.